J. Am. Soc. Mass Spectrom. (2014) 25:1237–1246
DOI: 10.1007/s13361-014-0882-3

RESEARCH ARTICLE

Analysis of the Lipidome of Xenografts Using MALDI-IMS and UHPLC-ESI-QTOF

Roberto Fernández,[1] Sergio Lage,[1,2] Beatriz Abad-García,[3] Gwendolyn Barceló-Coblijn,[4] Silvia Terés,[5] Daniel H. López,[4] Francisca Guardiola-Serrano,[6] M. Laura Martín,[7] Pablo V. Escribá,[6] José A. Fernández[1]

[1]Department of Physical Chemistry, Faculty of Science and Technology, University of the Basque Country (UPV/EHU), Barrio Sarriena s/n, 48940, Leioa, Spain
[2]Metabolism Unit, Department of Paediatrics, Cruces University Hospital, Plaza de Cruces s/n, 48903, Barakaldo, Vizcaya, Spain
[3]Central Analysis Service, Faculty of Science and Technology, University of the Basque Country (UPV/EHU), Barrio Sarriena s/n, 48940, Leioa, Spain
[4]Lipids in Human Pathology, Research Unit, Hospital Universitari Son Espases, Palma Health Research Institute, Carretera de Valldemossa 79, E-07010, Palma, Balearic Islands, Spain
[5]Unité de recherche Inserm 0916, Institut européen de chimie et biologie (IECB)-INSERM, 2, rue Robert Escarpit, 33607, Pessac, France
[6]Laboratory of Molecular Cell Biomedicine, Department of Biology, University Institute for Research into Health Sciences (IUNICS), University of the Balearic Islands, 07122, Palma, Balearic Islands, Spain
[7]Laboratory of Signal Transduction, Memorial Sloan-Kettering Cancer Center, 415 East 68th Street, New York, NY 10065, USA

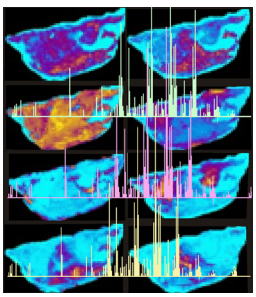

Abstract. Human tumor xenografts in immunodeficient mice are a very popular model to study the development of cancer and to test new drug candidates. Among the parameters analyzed are the variations in the lipid composition, as they are good indicators of changes in the cellular metabolism. Here, we present a study on the distribution of lipids in xenografts of NCI-H1975 human lung cancer cells, using MALDI imaging mass spectrometry and UHPLC-ESI-QTOF. The identification of lipids directly from the tissue by MALDI was aided by the comparison with identification using ESI ionization in lipid extracts from the same xenografts. Lipids belonging to PCs, PIs, SMs, DAG, TAG, PS, PA, and PG classes were identified and their distribution over the xenograft was determined. Three areas were identified in the xenograft, corresponding to cells in different metabolic stages and to a layer of adipose tissue that covers the xenograft.

Key words: Imaging mass spectrometry, Lipidomics, Human lung cancer, Xenografts, UHPLC, MALDI

Received: 28 January 2014/Revised: 10 March 2014/Accepted: 10 March 2014/Published online: 24 April 2014

Introduction

Since the introduction of imaging mass spectrometry (IMS)[1–6], it has become a technique of reference to determine the distribution of proteins [7–14], lipids [15–31], drugs [32–39], and metabolites [32, 40–50] in tissues of very different origin, attributable to several advantages that it presents compared with other traditional image techniques, such as radiography or fluorescence labeling: very little sample preparation is required, data acquisition is fast, there is no need for a priori labeling and, therefore, many unknowns may be detected, and the large dynamic range of the technique allows for detection of numerous species in a single run [51], although some ion suppression process may exist because of the interference between species [52]. Therefore, it is advisable to complement the results with those obtained by LC/MS.

Indeed, UHPLC-MS (ultra-high performance liquid chromatography-mass spectrometry) is becoming a reference technique in metabolomics and more specifically in lipidomics [53–60]; the separation provided by the chromatography adds another dimension to the analysis. In addition to the value of

Electronic supplementary material The online version of this article (doi:10.1007/s13361-014-0882-3) contains supplementary material, which is available to authorized users.

Correspondence to: José Fernández; *e-mail:* josea.fernandez@ehu.es

the mass, the UHPLC gives the retention time, which may be used to classify the lipids and to solve difficult assignments. Several works have already been published in which identification of lipids in the sample is complemented with the information obtained by UHPLC-MS [55–60]. Here, we combine the two techniques in the analysis of xenograft of NCI-H1975 human lung adenocarcioma.

Xenograft is one of the most popular murine models to investigate human cancer and to examine the responses to new treatments [61–68]. In this model, human tumor cells are transplanted either under the skin or into the organ type in which the tumor originated of immunocompromised (nude) mice that do not reject human cells. Tumors may develop within 1 to 8 wk and the response to new drugs can be then studied in vivo [69]. In this sense, xenografts have been widely used to test new drugs [70–73]. One of the main advantages of this model is that the response to the treatment is evaluated in human-originated cells, in a more physiological context than in a culture dish.

Several methods are commonly used to follow the evolution of a xenograft after treatment with a drug candidate. Usually, changes in vivo in tumor size, which are an indicator of the drug efficacy, are assessed by digital calipers or less common but more sophisticated, by micro-computed tomography [74]. In addition, changes in expression level of proliferation markers may be followed by specific fluorescent probes injected into the animal and visualized by noninvasive imaging methods. Once the xenograft is isolated, tissue sections can be prepared and the topological changes in protein expression levels may be evaluated by immunohistochemistry techniques.

There is currently an increased interest in the role that lipids play in cancer. In this sense, the evaluation is usually done using UHPLC-MS, which allows for a thorough description of the xenograft lipid composition. However, local changes associated with differences in metabolism or in cell differentiation degree within the xenograft may be missed. This is particularly relevant in the context of studies on drug response mechanisms, and it could be overcome by analyzing xenograft sections by IMS.

Here we use UHPLC-MS to obtain a detailed description of the lipidome, while MALDI-IMS will provide information on the distribution of some (or most) of the lipid species. Comparison between the outcomes of both techniques will allow us to evaluate the heterogeneity of the tumor and the possible existence of cells in different metabolic stages.

The procedure will be as follows: three xenografts of human lung cancer were extracted 8 wk after the subcutaneous cell injection. Part of the sample was used for lipid extraction and UHPLC-MS^E analysis, whereas the rest was used for sectioning and MALDI-IMS analysis. Comparison between the results from the two techniques is then carried out to determine the distribution of phosphatidylcholine (PC), phosphatidylethanolamine (PE), phosphatidylinositol (PI), phosphatidylglycerol (PG), phosphatidylserine (PS), phophatidic acid (PA), sphingomyelin (SM), diacylglycerol (DAG), and triacylglycerol (TAG) lipid classes, and to identify the maximum number of species.

Materials and Methods

Chemical reagents, description of animal, and tumor grafts may be found in the online resources. Lipid extracts were performed by the Bligh and Dyer method [75], while matrix was deposited using a sublimator [76–78] (see online resources for a description of the procedures).

MALDI-IMS

At least three sections of each sample were scanned, both in positive and negative ion detection modes, at spatial resolutions between 100 and 150 μm, using the Orbitrap analyzer of an LTQ-Orbitrap XL (ThermoFisher, San Jose, CA, USA), equipped with an N_2 laser (100 μJ max power, 50 μm spot diameter, 60 Hz repetition rate). Owing to the amorphous nature of the sample, no anatomical structures were observed at any of the spatial resolutions employed. Mass resolutions of 60,000 and 100,000 were used to record the data, and the scanning range was 400–1000 both in positive and negative modes.

The spectra were analyzed using dedicated software (MSIAnalyst; NorayBioinformatics S.L., Derio, Spain). During parsing, the size of the data was reduced, eliminating all the peaks with intensity lower than the 1% of the strongest peak on the spectrum, and the spectra were normalized using a total ion current algorithm [79]. Spectra were also aligned using the method of Xiong et al. [80] and assuming a maximum misalignment of 0.02 u, which is very conservative for an Orbitrap analyzer. During graphical representation, no interpolation or smoothing algorithms or any de-noizing procedure was used, always trying to maintain the original aspect of the data.

Statistical analysis was carried out using principal component analysis (PCA) [81] and k-means [82], a clustering procedure, taking into account all the mass-channels in the spectrum that survived the parsing stage. The second procedure shows a significantly better performance and, therefore, the results from the PCA analysis will not be shown here.

Lipid identification in MALDI-IMS is based on a direct comparison between the value of the *m/z* and the lipids in the software's lipid data base (>33,000 species plus their adducts) and with those in the Lipid Maps data base (www.lipidmaps.org). Mass accuracy is always better than 5 ppm and is typically better than 3 ppm. In those cases where no univocal assignment was found, a comparison with the data from UHPLC was performed. If a candidate was not detected by UHPLC-MS, and it was not detected as another adduct in the MALDI-IMS experiment, such candidate was removed from the list.

UHPLC-MS^E Analysis

Ultrahigh performance liquid chromatography (UHPLC) was carried out by using an ACQUITY UPLC system from Waters (Milford, MA, USA), equipped with a binary solvent delivery pump, an autosampler, and a column oven. The

extracts were injected onto a column (Acquity UPLC HSS T3 1.8 µm, 100×2.1 mm) from Waters, which was heated to 65ºC. Mobile phases consisted of acetonitrile and water with 10 mM ammonium acetate (40:60, v/v) (phase A) and acetonitrile and isopropanol with 10 mM ammonium acetate (10:90, v/v) (phase B). Separation was carried out in 13 min under the following conditions: 0–10 min, linear gradient from 40% to 100% B; 10–11 min, 100% B; and finally, re-equilibration of the system with 40% B (v/v) for 2 min prior to the next injection. Flow rate was 0.5 mL/min and injection volume was 5 µL. All samples were kept at 4ºC during the analysis.

All UHPLC-MS^E data were acquired on a SYNAPT G2 HDMS, with a quadrupole time of flight (Q-ToF) configuration, (Waters) equipped with an electrospray ionization (ESI) source that can be operated in both positive and negative modes. The capillary voltage was set to 0.7 kV (ESI+) or 0.5 kV (ESI−). Nitrogen was used as desolvation and cone gas, at flow rates of 900 L/h and 30 L/h, respectively. The source temperature was 120ºC, and the desolvation temperature was 400ºC.

Leucine-enkephalin solution (2 ng/µL) in acetonitrile:water (50:50 (v/v) + 0.1% formic acid) was utilized for the lock-mass correction and the ions at mass-to-charge ratios (*m/z*) 556.2771 and 278.1141, or 554.2615 and 236.1035, depending on the ionization mode, from this solution, were monitored at scan time 0.3 s, and at 10 s intervals, 3 scans on average, using a mass window of ±0.5 Da. The rest of the conditions were: lockspary capillary 2.0 and 2.5 kV and collision energy 21 and 30 eV in ESI+or ESI–, respectively. The reference internal calibrant was introduced into the lock mass sprayer at a constant flow rate of 10 µL/min, using an external pump.

All acquired spectra were automatically corrected during acquisition using the lock mass. Before analysis, the mass spectrometer was calibrated with a sodium formate 0.5 mM solution.

Data acquisition took place over the mass range 50–1200 u in resolution mode (FWHM≈20,000) with a scan time of 0.5 s and an inter-scan delay of 0.024 s. The mass spectrometer was operated in the continuum MS^E acquisition mode for both polarities. During this acquisition method, the first quadrupole Q1 is operated in a wide band rf mode only, allowing all ions to enter the T-wave collision cell. Two discrete and independent interleaved acquisition functions were automatically created: the first function, typically set at 6 eV, collected low energy or unfragmented data, whereas the second function collected high energy or fragmented data typically obtained by using a collision energy ramp from 15–40 eV. In both cases, Ar gas was used for collision induced dissociation (CID).

Data processing and lipid identification procedures may be found in the online resources.

Results and Discussion

Figure 1 shows the images created using some of the mass channels in the spectra from one of the xenograft sections in positive mode detection, whereas Supplementary Figure S1 (Supporting Information) shows the same kind of images but using the *m/z* channels in the spectra recorded using negative detection. It is clear from both sets of images that there are three well-defined areas: a triangular one in the center of the figure (for example the distribution of *m/z* =789.492), a second one composed of two "hot spots" (e.g., *m/z*= 739.474), and a third one that defines the rim of the tissue (e.g., 907.776), and that it is difficult to visualize in Figure 1 and Supplementary Figure S1, but that it is clearly seen in the statistical analysis (see below). Some lipids can be found only in one of the three areas, while others are distributed along the whole tissue, like *m/z*=816.594.

A significantly smaller number of species is detected in negative mode. This may be due to the matrix employed: it is well-known that MBT gives an excellent intensity in positive mode, but its performance in negative detection is not optimal [76]. However, the number of species detected should be enough to compare with the results from UHPLC-MS^E. Furthermore, comparison between the images on Figure 1 and Supplementary Figure S1 demonstrate that the same areas are found in both detection modes.

The areas in the tissue do not seem to be due to differences in ionization efficiencies, as some lipids are almost evenly distributed along the whole tissue, but to real differences in the distribution. Thus, they may correspond to a portion of the tumor containing cells at different metabolic or developmental stage.

Figure 2 shows the three areas found using the clustering procedure described in the Methods section, together with the average spectrum over each of the three areas. Most of the tissue is covered by clusters 1 and 2, whereas cluster 3 defines a thin line around the tissue and a narrow line in the upper-right part of the section. The general intensity of the spectrum of this cluster is lower than in the other two clusters. A group of peaks at high masses is also evident, which correspond mainly to TAGs. The average spectrum over the whole tissue is also shown for comparison. As can be seen, the average spectrum of cluster 2 presents a higher intensity. Several strong peaks change their intensity between clusters 1 and 2 but, in general, a higher abundance of peaks is observed in cluster 2. Annotated average spectra may be found in Supplementary Figures S3 and S4 of the online resources.

The average spectrum obtained in negative mode presents a significantly smaller number of peaks. Although the positive mode spectrum is usually dominated by LPCs, DAGs, PCs, SMs, and TAGs and PIs in the high-mass side, a larger number of lipid classes is usually found with negative detection, such as PAs, PEs, PGs, PS, sulfatides or PIs. Thus, either such classes are not present in high-enough concentration to be detected in the MALDI-IMS experiment or the matrix employed does not allow their detection.

The advantage of UHPLC-ESI-MS over MALDI-MS is the introduction of a separation stage before the analysis of the lipids. Figure 3 shows the chromatograms obtained in

Figure 1. Images built integrating the *m/z* channels in the spectra of a section of a xenograft recorded in positive mode, and representing them against the coordinates at which the spectra were acquired. MBT was used as matrix. Ten shots were averaged for each spectrum, with a laser intensity of 6 μJ/pulse. The pixel size was 150 μm and the spectra were recorded with the Orbitrap analyzer at 100,000 resolution. Each image contains 6887 pixels. The color scale is also shown

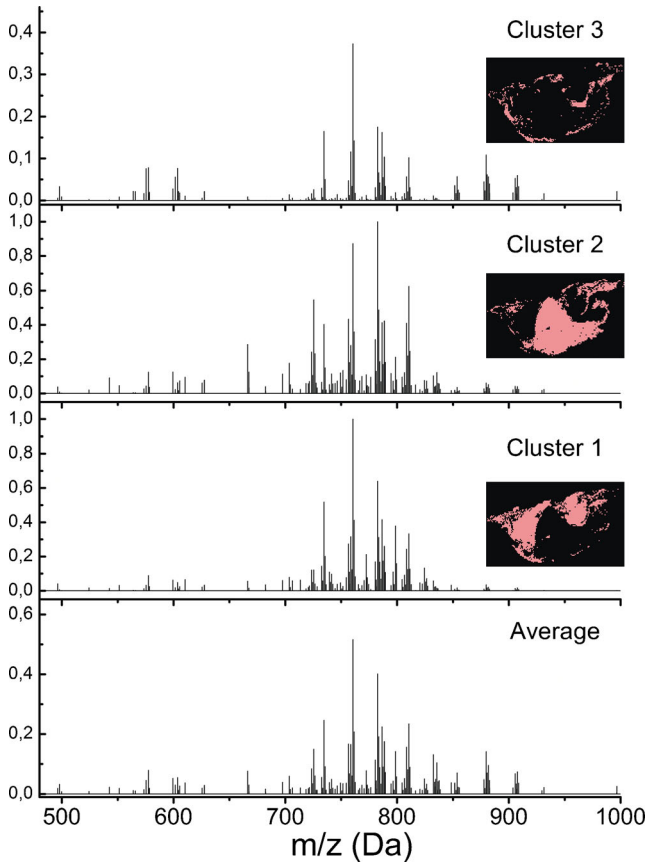

Figure 2. Comparison between the average spectra over each of the three clusters in which the K-means algorithm groups the spectra and the average spectrum over the whole tissue section, recorded in positive mode. The regions in each cluster are also shown as inserts

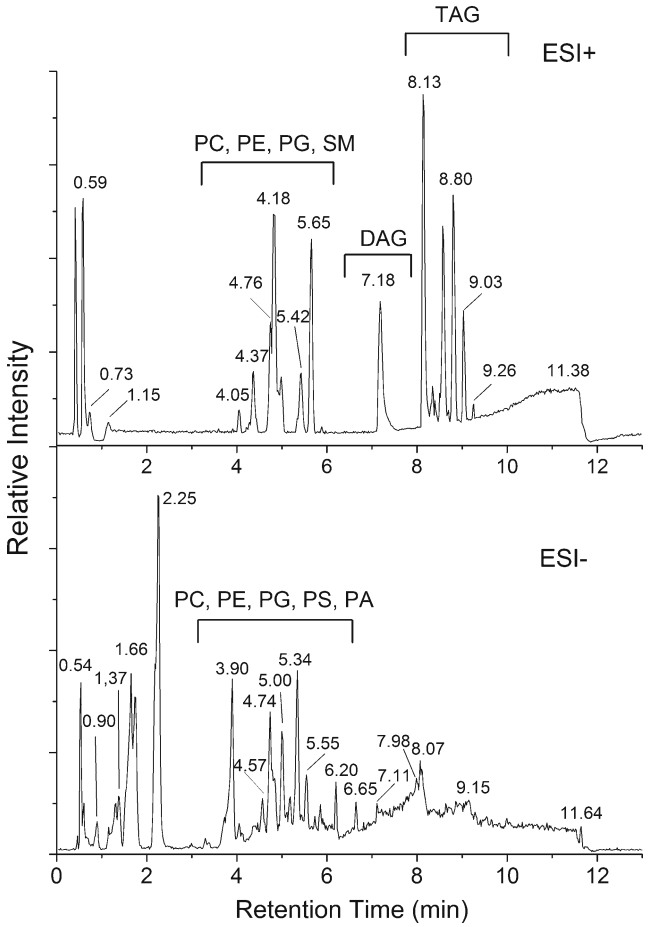

Figure 3. UHPLC chromatograms ESI + (upper panel), ESI– (lower panel), of lipid extracts from xenografts of human lung cancer

positive and negative detection modes when an extract of the lipids in the xenograft is injected. As can be seen, when ESI + mode is used, the glycerophospholipids appear at retention times of ~4–5 min, whereas less polar lipids (DAGs and TAGs) appear at longer retention times. In negative mode, it is possible to isolate the fatty acids (FA) from the glycerophospholipids, which appear at longer retention times. Furthermore, each lipid class presents a characteristic retention time, as demonstrated by the chromatograms collected in Supplementary Tables S8 and S9 of the online resources. When the information from fragmentation is added (Supplementary Figures S5–S11 of the online resources), a very precise identification of the lipid species in the extract can be achieved.

Table 1 and Supplementary Tables S1–S9 collect the species detected in the present work, using either MALDI or ESI, together with the adducts found for each species and the distribution along the tissue, for those species detected using MALDI-IMS; 29 mass/channels (54 if the different adducts are taken into account) may be assigned to PC species in the MALDI-IMS experiment (Table 1), and 27 (73 if the different adducts are taken into account) using ESI. The intensity of 15 species was high enough to allow recording the MS/MS spectra and, therefore, the composition of the acylic chains is also offered in the table.

As can be seen from the table, most of the species were detected by both ionization methods. The differences encountered may be due to a better sensitivity in MALDI, probably due to the excellent performance of MBT in the detection of phospholipids in positive mode. Also, some of the *m/z* in the MALDI spectra may be assigned to several species that were also detected by ESI (e.g., PC(O-34:2)+H^+/PC(P-34:0)+H^+), which means that very likely the *m/z* contains the contribution from all the overlapping species. Therefore, the distribution map obtained for such channel is the distribution of several species together.

It is worthy to note that the abundance of plasmalogens among the PCs was higher than the number of such species usually found in normal tissue using IMS [51, 83]. While the data in the literature point to a contribution of ~1% of the plasmalogens to the total amount of PCs in lung, around a 13% is found in the present work. Furthermore, they are mainly located in the area defined by cluster 2. Interestingly, the comparison with the lipids detected in colon adenocarcinoma cells shows that a similar amount of plasmalogens is found [84]. Abundant plasmalogens were also found in

Table 1. Comparison Between the PC Species Detected by MALDI and ESI

Species	Adduct		Tentative structure
	MALDI	ESI	
30:0	$+H^+_{(1)}$	$+H^+$, $+AcO^-$,$-CH3^+$	PC(14:0/16:0)/ PC(16:0/14:0)
O-32:1	$+H^+_{(2)}$, $+Na^+_{(2)}$	$+H^+$	
32:1	$+H^+_{(1)}$, $+K^+_{(1)}$	$+H^+$, $+AcO^-$,$-CH3^+$	PC(16:0/16:1)
O-32:0	$+H^+_{(2)}$, $+Na^+_{(2)}$	$+H^+$	
32:0	$+H^+_{(1+2)}$, $+K^+_{(1)}$ [a]	$+H^+$, $+Na^+$, $+K^+$, $+AcO^-$,$-CH3^+$	PC(16:0/16:0)
33:1	$+H^+_{(1)}$	$+H^+$, $+Na^+$, $+AcO^-$	
O-34:2/P-34:1	$+H^+_{(2)}$/ $+H^+_{(2)}$	$+H^+$/+ H^+	
P-34:0	$+H^+_{(2)}$	$+H^+$, $+AcO^-$	PC(P-16:0/18:0)
34:2	$+H^+_{(3)}$, $+Na^+_{(2+3)}$, $+K^+_{(1)}$ [b]	$+H^+$, $+Na^+$, $+K^+$, $+AcO^-$,$-CH3^+$	PC(16:0/18:2)
34:1	$+H^+_{(3)}$, $+K^+_{(1)}$	$+H^+$, $+Na^+$, $+K^+$, $+AcO^-$,$-CH3^+$	PC(16:0/18:1)
34:0	$+H^+_{(1)}$, $+K^+_{(1)}$	$+H^+$, $+Na^+$, $+K^+$,$+AcO^-$,$-CH3^+$	PC(16:0/18:0)
O-36:5/P-36:4	$+H^+_{(1+2+3)}$, $+Na^+_{(2+3)}$/ $+H^+_{(1+2+3)}$, $+Na^+_{(2+3)}$	$+H^+$,$+AcO^-$/ $+H^+$, $+AcO^-$	
O-36:4/P-36:3	$+H^+_{(1+2+3)}$, $+Na^+_{(2)}$/ $+H^+_{(1+2+3)}$, $+Na^+_{(2)}$	$+H^+$/ $+H^+$	
O-36:3/P-36:2	$+H^+_{(3)}$/ $+H^+_{(3)}$	$+H^+$/ $+H^+$	
O-36:2/P-36:1	$+H^+_{(3)}$, $+Na^+_{(2)}$[c]/ $+H^+_{(3)}$, $+Na^+_{(2)}$[c]	$+H^+$ / $+H^+$	
O-36:1	$+Na^+_{(2)}$[d]		
36:4	$+H^+_{(2+3)}$, $+K^+_{(1)}$	$+H^+$, $+Na^+$, $+K^+$, $+AcO^-$,$-CH3^+$	PC(16:0/20:4)
36:3	$+H^+_{(3)}$, $+Na^+_{(2+3)}$, $+K^+_{(1)}$	$+H^+$, $+Na^+$, $+K^+$, $+AcO^-$,$-CH3^+$	PC(16:0/20:3)
36:2	$+H^+_{(3)}$, $+Na^+_{(1+2+3)}$, $+K^+_{(1)}$	$+H^+$, $+Na^+$, $+K^+$, $+AcO^-$,$-CH3^+$	PC(18:0/18:2)
36:1	$+H^+_{(2)}$, $+Na^+_{(2+3)}$,$+K^+_{(1)}$	$+H^+$, $+Na^+$, $+K^+$,$+AcO^-$,$-CH3^+$	PC(18:0/18:1)
O-38:5/P-38:4	$+H^+_{(2)}$, $+Na^+_{(1+2+3)}$/ $+H^+_{(2)}$, $+Na^+_{(1+2+3)}$	$+H^+$/+ H^+	
O-38:4/P-38:3	$+H^+_{(2)}$, $+Na^+_{(2)}$/ $+H^+_{(2)}$, $+Na^+_{(2)}$	$+H^+$/+ H^+	
38:6	$+K^+_{(1)}$	$+H^+$	
38:5	$+H^+_{(1+2+3)}$, $+K^+_{(1)}$	$+H^+$,$+AcO^-$	PC(16:0/22:5)
38:4	$+H^+_{(2+3)}$, $+Na^+_{(3)}$, $+K^+_{(1)}$	$+H^+$, $+Na^+$, $+K^+$,$+AcO^-$,$-CH3^+$	PC(16:0/22:4)
38:3	$+H^+_{(1+2)}$, $+Na^+_{(3)}$	$+H^+$,$+AcO^-$	PC(18:0/20:3)
38:2	$+Na^+_{(3)}$		
40:6	$+H^+_{(3)}$	$+H^+$	
40:5	$+H^+_{(3)}$		
40:4		$+H^+$	PC(18:0/22:4)

When more than one species may correspond to the same *m/z* they are separated by "/". Different adducts of each species are separated by ",". The subscript indicates in which cluster of Figure 3 the species appear.

[a] Overlaps with: $[PE\ (O\text{-}38:6)+Na]^+$.

[b] Overlaps with: $[PE\ (P\text{-}40:7)+H]^+$/$[PE\text{-}NMe\ (36:2)+K]^+$/$[PE\ (37:2)+K]^+$.

[c] Alternative assignment: $[PE\ (P\text{-}39:1)+Na]^+$.

[d] Alternative assignment: $[PE\ (O\text{-}39:1)+Na]^+$/$[PE\ (P\text{-}39:0)+Na]^+$.

malignant glioma cell lines using FTICR [85]. Furthermore, such increase was also found in patients with breast, lung, and prostate cancer [86]. Plasmalogen synthesis involves two different cell organelles: peroxisomes in which the ether linkage is formed, and the endoplasmic reticulum where, in case of the alkenyl subclass, the double bond of the vinyl ether linkage is inserted. Because some peaks cannot be unambiguously assigned to alkyl- or to alkenyl-PC molecular species as they overlap in molecular mass, the alteration in plasmalogen mass may be due to changes in the enzymatic activity at any of the two stages of the synthesis.

As can be seen, it is not easy to find the metabolic mechanism behind such increase in plasmalogens in tumor tissue but several works point to the existence of a connection. It is well known that there is a deregulation of the lipids metabolism in cancer [87]. Indeed, cancer cells reprogram their metabolism for their abnormal proliferation. Therefore, an overabundance of plasmalogens may be the signature of the existence of tumors, opening the door to identify biomarkers for a wide spectrum of cancers.

The subscripts in the second column of Tables 1, 2, and Supplementary Tables S1–S7 indicate in which cluster (or clusters) a given species is found. A table with each species, the image built integrating its mass channel and its chromatogram, can be found in Supplementary Tables S8 and S9 of the online resources. It is clear from Table 1 that some lipids exhibit a preferential location in one of the three clusters, whereas others are found over the whole tissue. However, the most striking observation is that the K^+ adducts are exclusively located in cluster 1. Differential distribution of adducts has already been reported in MALDI-IMS of rat brain sections of an ischemia model [88]. In that study, a higher abundance of Na^+ adducts was found in the damaged areas of the brain, and it was interpreted on the basis of a change in activity of the Na+/K+-ATPase.

A similar comparison is performed in Table 2 for PE species. In the MALDI experiments, most of the PE species were detected in positive mode, whereas in ESI, almost all of the PE species were detected in negative mode. The ion suppression in MALDI positive mode is probably responsible for the lower number of species detected using this ionization form. Similar to what is observed for PCs, a significant number of plasmalogens were detected, following the same trend observed in other studies on the lipidome of

Table 2. Comparison Between the PE Species Detected by MALDI and ESI

Species	Adduct		Tentative structure
	IMS	ESI	
PE-NMe_2(34:1)		$+AcO^-$	
PE-NMe_2 (32:0)/34:0	$-H^+_{(2)}$/ $-H^+_{(2)}$	$-H^+$,+ AcO^-/$-H^+$, $+AcO^-$	
O-34:4/P–34:3	$+ Na^+_{(2)}$		
P-34:2		$+H^+$, $-H^+$	PE(P-16:0/18:2)
P-34:1		$+H^+$, $- H^+$	PE(P-16:0/18:1)
34:1		$+H^+$,$-H^+$	PE(16:0/18:1)
35:2		$+AcO^-$	
35:0	$+ Na^+_{(1+2+3)}$	$+AcO^-$	
P-36:4		$+H^+$, $+Na^+$, $-H^+$	PE(P-16:0/20:4)
P-36:2		$+H^+$, $-H^+$	PE(P-18:0/18:2)
P-36:1		$+H^+$, $-H^+$	PE(P-18:0/18:1)
36:3/34:0	$+ H^+_{(1)}$/$+ Na^+_{(1)}$	$-H^+$/$-H^+$	
36:2	$-H^+_{(2)}$	$-H^+$, $+AcO^-$	PE(18:0/18:2)
36:1	$-H^+_{(2)}$	$+H^+$, Na^+, $-H^+$, $+AcO^-$	PE(18:0/18:1)
37:4/35:1	$+ H^+_{(3)}$/$+ Na^+_{(3)}$	$+AcO^-$/$+AcO^-$	
O-38:6	$Na^+_{(1)}$[a]	$-H^+$, $-H^+$	PE(O-16:0/22:6)
P-38:6		$+H^+$, $-H^+$	PE(P-16:0/22:6)
P-38:4		$+H^+$, $-H^+$/$+H^+$, $+Na^+$, $-H^+$	PE(P-18:0/20:4)/ PE(P-16:0/22:4)
38:6		$-H^+$	PE(16:0/22:6)
38:4		$+ H^+$, $+ Na^+$, $-H^+$	PE(18:0/20:4)
38:2/ PE-NMe_2 (36:2)	$-H^+_{(2)}$/$-H^+_{(2)}$	$+AcO^-$/$+AcO^-$	
38:1	$-H^+_{(1+2)}$	$+AcO^-$	
O-39:1/P-39:0	$+ Na^+_{(2)}$[d]/$+ Na^+_{(2)}$[d]		
P-39:1	$+ Na^+_{(2)}$[b]		
O-40:6		$+H^+$,$-H^+$	PE(O-18:0/22:6)
P-40:7	$+ Na^+_{(1)}$[c]	$+H^+$, $-H^+$	PE(P-18:1/22:6)
P-40:6		$+H^+$, $-H^+$	PE(P-18:0/22:6)
P-40:4		$+H^+$, $-H^+$	PE(P-18:0/22:4)
40:6		$+H^+$, $-H^+$	PE(18:0/22:6)
40:4	$+ H^+_{(2)}$	$+H^+$, $-H^+$	PE(18:0/22:4)
41:2	$+ Na^+_{(2+3)}$		

When more than one species may correspond to the same *m/z*, they are separated by "/". Different adducts of each species are separated by ",". The subscript indicates in which cluster(s) of Figure 3 the species appear.
[a] Overlaps with: $[PC\ 32:0)+K]^+$.
[b] Alternative assignment: $[PC\ (O\text{-}36:2)+Na]^+$.
[c] Overlaps with: $[PC\ (34:2)+K]^+$.
[d] Alternative assignment: $[PC\ (O\text{-}36:1)+Na]^+$.

tumors [84]. The composition of the acylic chains is also collected in the table for those species with high-enough intensity to allow recording their MS/MS spectrum.

Regarding localization of the PE species, K^+ adducts are almost exclusively found in cluster 1, whereas the rest of adducts has a higher propensity to appear in cluster 2, which occupies the central part of the tumor.

Following with the rest of the glycerophospholipids, the PI species detected are summarized in Supplementary Table S1. The number of species is lower than in Tables 1 and 2, but still 15 species were detected in MALDI, whereas 11 species were detected using ESI. As can be seen in Supplementary Table S1, the agreement between both techniques is remarkable. Against what was observed for PCs and PEs, the PIs are distributed along the whole tissue

It is well known that PIs usually give a strong signal and normally dominate the MALDI spectrum in negative mode, together with STs, when present, whereas the rest of the glycerophospholipids, PAs, PGs, and PSs, are more difficult to detect in MALDI. Such fact is also reflected in Supplementary Tables S2–S4. Of these three classes, only PAs seem to be present in a significant amount. However, a close inspection of the species identified shows that most of them are coincident with alternative assignments, mainly DAGs and PIs and, therefore, such assignments must be taken with caution.

Supplementary Table S5 collects the detected species of SM. Nine different SM were found using MALDI, while nine species were also found using ESI ionization. As can be seen, the agreement between both sets of data is also excellent. It is worthy to note that all the species are almost exclusively found in the area defined by cluster 2.

Finally, Supplementary Tables S6 and S7 show the DAG and TAG species that were found. Although a large number of TAGs seems to be present, very few DAGs were found: only seven species using MALDI and nine species using ESI. Furthermore, both sets of data do not match, which challenges the assignment. One must take into account that the TAGs may fragment during MALDI ionization and show up in a DAG mass-channel, leading to a wrong assignment. Thus, the MALDI data in Supplementary Table S6 must be taken with caution.

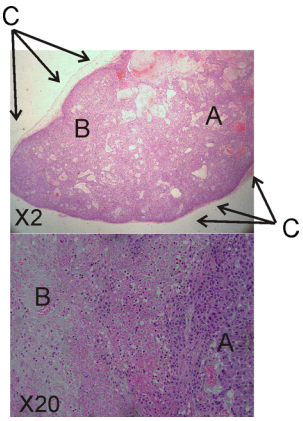

Figure 4. Microscopic appearance (×2, ×20) of a histologic sections of xenograft of A549 cells stained with hematoxiline and eosine. In the upper panel, viable areas (**a**) and necrotic areas (**b**) as well as the surrounding connective and adipose tissue (**c**) can be observed. In the lower panel, a higher magnification allows to distinguish viable cells (A, bigger and darker nuclei) and non-viable cells (B, smaller nuclei because chromatin condensation)

On the other hand, the data in Supplementary Table S7 on the detection of TAGs show a very different landscape: numerous species were detected by both techniques, but especially by ESI. The assignment is very solid because most of the species were detected forming three different adducts. Interestingly, almost all TAGs were detected in cluster 3 (i.e., in the outer part of the xenograft) and may be due to fatty tissue generated by the mouse to protect itself from the tumor.

In fact, once cells are injected subcutaneously into the mouse, the host tissue tends to pseudo-encapsulate as it is recognized as a foreigner entity. So, the growing tumor is usually surrounded by a number of layers of connective and adipose tissue, which would perfectly account for the TAG distribution observed by IMS and the increase in TAG observed by ESI (Figure 4).

As mentioned above, two different areas are observed in the section in Figure 4: one, denoted in the figure as A, with viable cells, and the other, denoted as B, with non-viable cells, which may have suffered for example, from a lack of irrigation. The existence of two areas fit very well with the observation of two distinct lipid distributions, defined as clusters 1 and 2 in Figure 2.

Conclusions

In this work, the lipid composition of xenografts of human lung adenocarcinoma NCI-H1975 cells has been analyzed using MALDI-IMS and UHPLC-ESI-TOF. Three tumor samples were used, offering consistent results and, therefore, they may be considered as representative of the kind of xenografts analyzed here.

The images generated from the different mass channels in the MALDI experiment demonstrate that the xenograft presents at least three well-defined regions with a characteristic lipid composition. In one of the regions, cluster 1, a lower abundance of species and a concentration of potassium adducts is found. In region 2, most of the PC plasmalogens and SMs are located. Comparison with the literature shows that an abundance of plasmalogens is usually found in tumor tissues of different origins. Further experiments are being conducted in our laboratory on different tumor tissues to test if such lipid class is a biomarker for the existence of tumors.

Finally, region 3 defines a rim around the tissue and may correspond to formation of connective tissue by the mouse's body to protect itself from the xenograft. Most of the TAG species are located in this frontier region, indicating that they may be from the mouse's connective and/or fatty tissue and, therefore, they may not be part of the xenograft.

The present results stress that both techniques are required for the understanding of complex samples such as tumor xenografts.

Acknowledgment

The authors thank Dr. Begoña Ochoa for her help with the assignment of the lipids in xenografts, and to the Basque Government for its support of the present project (SAIOTEK). Technical support and personnel provided by the *Servicio de Lipidómica* of the SGIKER (UPV/EHU, MICINN, GV/E.G., ESF) is gratefully acknowledged. G.B.-C. holds a'Miguel Servet'contract from the Instituto Carlos III, Ministerio de Economía y Competitividad. S.T. holds a contract from the INSERM (Institut National de la santé et de la recherche médical). Délégation regional de Bordeaux.

References

1. Spengler, B., Hubert, M., Kaufmann, R.: MALDI Ion Imaging and Biological Ion Imaging with a New Scanning UV-Laser Microprobe. Proceedings of the 42nd Annual Conference on Mass Spectrometry and Allied Topics, pp. 1041, Chicago, IL (1994)
2. Stoeckli, M., Chaurand, P., Hallahan, D.E., Caprioli, R.M.: Imaging mass spectrometry: a new technology for the analysis of protein expression in mammalian tissues. Nat Med **7**(4), 493–496 (2001)
3. Todd, P.J., Schaaff, T.G., Chaurand, P., Caprioli, R.M.: Organic ion imaging of biological tissue with secondary ion mass spectrometry and matrix-assisted laser desorption/ionization. J Mass Spectrom **36**(4), 355–369 (2001)
4. Chaurand, P., Stoeckli, M., Caprioli, R.M.: Direct profiling of proteins in biological tissue sections by MALDI mass spectrometry. Anal Chem **71**(23), 5263–5270 (1999)
5. Caprioli, R.M., Farmer, T.B., Zhang, H.Y., Stoeckli, M.: Molecular imaging of biological samples by MALDI MS. Abstracts of Papers of the American Chemical Society **214**, 113–ANYL (1997)
6. Caprioli, R.M., Farmer, T.B., Gile, J.: Molecular imaging of biological samples: localization of peptides and proteins using MALDI-TOF MS. Anal Chem **69**(23), 4751–4760 (1997)
7. Pierre, S., Scholich, K.: Toponomics: studying protein–protein interactions and protein networks in intact tissue. Mol. Biosys. **6**(4), 641–647 (2010)
8. Franck, J., Longuespee, R., Wisztorski, M., van Remoortere, A., Van Zeijl, R., Deelder, A., Salzet, M., McDonnell, L., Fournier, I.: MALDI mass spectrometry imaging of proteins exceeding 30,000 daltons. Med. Sci. Monitor **16**(9), BR293–BR299 (2010)

9. Stauber, J., MacAleese, L., Franck, J., Claude, E., Snel, M., Kaletas, B.K., Wiel, I.M.V.D., Wisztorski, M., Fournier, I., Heeren, R.M.A.: On-tissue protein identification and imaging by MALDI-ion mobility mass spectrometry. J Am Soc Mass Spectrom **21**(3), 338–347 (2010)
10. Lim, S., Na, C., Lee, S., Kim, W., Chae, C., Kim, K.: Spatial identification of the proteins from renal cell carcinomas by imaging mass spectrometry. Virchows Arch **455**, 148–149 (2009)
11. Grey, A.C., Chaurand, P., Caprioli, R.M., Schey, K.L.: MALDI imaging mass spectrometry of integral membrane proteins from ocular lens and retinal tissue. J Proteome Res **8**(7), 3278–3283 (2009)
12. Burnum, K.E., Frappier, S.L., Caprioli, R.M.: Matrix-assisted laser desorption/ionization imaging mass spectrometry for the investigation of proteins and peptides. Annu Rev Anal Chem **1**, 689–705 (2008)
13. Andersson, M., Groseclose, M.R., Deutch, A.Y., Caprioli, R.M.: Imaging mass spectrometry of proteins and peptides: 3D volume reconstruction. Nat Methods **5**(1), 101–108 (2008)
14. Seeley, E.H., Caprioli, R.M.: Molecular imaging of proteins in tissues by mass spectrometry. Proc Natl Acad Sci USA **105**(47), 18126–18131 (2008)
15. Veloso, A., de San Roman, E.G., Astigarraga, E., Barreda-Gome, G., Manuel, I., Giralt, M.T., Ochoa, B., Fresnedo, O., Fernandez, J.A., Rodriguez-Puertas, R.: Anatomical distribution of lipids in human brain by imaging mass spectrometry. Chem Phys Lipids **163**, S3 (2010)
16. Eberlin, L.S., Ifa, D.R., Wu, C., Cooks, R.G.: Three-dimensional vizualization of mouse brain by lipid analysis using ambient ionization mass spectrometry. Angew Chem Int Ed **49**(5), 873–876 (2010)
17. Meriaux, C., Franck, J., Wisztorski, M., Salzet, M., Fournier, I.: Liquid ionic matrixes for MALDI mass spectrometry imaging of lipids. J. Proteom. **73**(6), 1204–1218 (2010)
18. Colsch, B., Woods, A.S.: Localization and imaging of sialylated glycosphingolipids in brain tissue sections by MALDI mass spectrometry. Glycobiology **20**(6), 661–667 (2010)
19. Goto-Inoue, N., Hayasaka, T., Zaima, N., Kashiwagi, Y., Yamamoto, M., Nakamoto, M., Setou, M.: The detection of glycosphingolipids in brain tissue sections by imaging mass spectrometry using gold nanoparticles. J Am Soc Mass Spectrom **21**(11), 1940–1943 (2010)
20. Deeley, J.M., Hankin, J.A., Friedrich, M.G., Murphy, R.C., Truscott, R.J.W., Mitchell, T.W., Blanksby, S.J.: Sphingolipid distribution changes with age in the human lens. J Lipid Res **51**(9), 2753–2760 (2010)
21. Veloso, A., Astigarraga, E., Barreda-Gomez, G., Manuel, I., Ferrer, I., Giralt, M.T., Ochoa, B., Fresnedo, O., Rodriguez-Puertas, R., Fernandez, J.A.: Anatomical distribution of lipids in human brain cortex by imaging mass spectrometry. J Am Soc Mass Spectrom **22**, 329–338 (2011)
22. Blanksby, S.J., Mitchell, T.W.: Advances in mass spectrometry for lipidomics. Annu Rev Anal Chem **3**, 433–465 (2010)
23. Hayasaka, T., Goto-Inoue, N., Zaima, N., Kimura, Y., Setou, M.: Organ-specific distributions of lysophosphatidylcholine and triacylglycerol in mouse embryo. Lipids **44**(9), 837–848 (2009)
24. Sugiura, Y., Konishi, Y., Zaima, N., Kajihara, S., Nakanishi, H., Taguchi, R., Setou, M.: Visualization of the cell-selective distribution of PUFA-containing phosphatidylcholines in mouse brain by imaging mass spectrometry. J Lipid Res **50**(9), 1776–1788 (2009)
25. Murphy, R.C., Hankin, J.A., Barkley, R.M.: Imaging of lipid species by MALDI mass spectrometry. J Lipid Res **50**, S317–S322 (2009)
26. Chan, K., Lanthier, P., Liu, X., Sandhu, J.K., Stanimirovic, D., Li, J.J.: MALDI mass spectrometry imaging of gangliosides in mouse brain using ionic liquid matrix. Anal Chim Acta **639**(1/2), 57–61 (2009)
27. Chen, R.B., Hui, L.M., Sturm, R.M., Li, L.J.: Three dimensional mapping of neuropeptides and lipids in crustacean brain by mass spectral imaging. J Am Soc Mass Spectrom **20**(6), 1068–1077 (2009)
28. Wang, H.Y.J., Jackson, S.N., Post, J., Woods, A.S.: A minimalist approach to MALDI imaging of glycerophospholipids and sphingolipids in rat brain sections. Int J Mass Spectrom **278**(2/3), 143–149 (2008)
29. Zheng, L., Mcquaw, C.M., Ewing, A.G.: Winograd, N: Sphingomyelin/phosphatidylcholine and cholesterol interactions studied by imaging mass spectrometry. J Am Chem Soc **129**(51), 15730–15731 (2007)
30. Malmberg, P., Nygren, H., Richter, K., Chen, Y., Dangardt, F., Friberg, P., Magnusson, Y.: Imaging of lipids in human adipose tissue by cluster ion TOF-SIMS. Microscop. Res. Technique **70**(9), 828–835 (2007)
31. Borner, K., Malmberg, P., Mansson, J.E., Nygren, H.: Molecular imaging of lipids in cells and tissues. Int J Mass Spectrom **260**(2/3), 128–136 (2007)
32. Trim, P.J., Francese, S., Clench, M.: Imaging mass spectrometry for the assessment of drugs and metabolites in tissue. Bioanalysis **1**, 309–319 (2010)
33. Goodwin, R.J.A., Scullion, P., MacIntyre, L., Watson, D.G., Pitt, A.R.: Use of a solvent-free dry matrix coating for quantitative matrix-assisted laser desorption ionization imaging of 4-bromophenyl-1,4-diazabicyclo(3.2.2)nonane-4-carboxylate in rat brain and quantitative analysis of the drug from laser microdissected tissue regions. Anal Chem **82**(9), 3868–3873 (2010)
34. Rowell, F., Hudson, K., Seviour, J.: Detection of drugs and their metabolites in dusted latent fingermarks by mass spectrometry. Analyst **134**(4), 701–707 (2009)
35. Cornett, D.S., Frappier, S.L., Caprioli, R.M.: MALDI-FTICR imaging mass spectrometry of drugs and metabolites in tissue. Anal Chem **80**(14), 5648–5653 (2008)
36. Hazarika, P., Jickells, S.M., Wolff, K., Russell, D.A.: Imaging of latent fingerprints through the detection of drugs and metabolites. Angew Chem Int Ed **47**(52), 10167–10170 (2008)
37. Wiseman, J.M., Ifa, D.R., Zhu, Y.X., Kissinger, C.B., Manicke, N.E., Kissinger, P.T., Cooks, R.G.: Desorption electrospray ionization mass spectrometry: imaging drugs and metabolites in tissues. PNAS **105**(47), 18120–18125 (2008)
38. Wang, H.Y.J., Jackson, S.N., McEuen, J., Woods, A.S.: Localization and analyses of small drug molecules in rat brain tissue sections. Anal Chem **77**(20), 6682–6686 (2005)
39. Liu, X., Ide, J.L., Norton, I., Marchionni, M.A., Ebling, M.C., Wang, L.Y., Davis, E., Sauvageot, C.M., Kesari, S., Kellersberger, K.A., Easterling, M.L., Santagata, S., Stuart, D.D., Alberta, J., Agar, J.N., Stiles, C.D., Agar, N.Y.R.: Molecular imaging of drug transit through the blood-brain barrier with MALDI mass spectrometry imaging. Sci. Rep. **3**, 6 (2013)
40. Nemes, P., Woods, A.S., Vertes, A.: Simultaneous imaging of small metabolites and lipids in rat brain tissues at atmospheric pressure by laser ablation electrospray ionization mass spectrometry. Anal Chem **82**(3), 982–988 (2010)
41. Solon, E.G., Schweitzer, A., Stoeckli, M., Prideaux, B.: Autoradiography, MALDI-MS, and SIMS-MS imaging in pharmaceutical discovery and development. AAPS J **12**(1), 11–26 (2010)
42. Manicke, N.E., Dill, A.L., Ifa, D.R., Cooks, R.G.: High-resolution tissue imaging on an orbitrap mass spectrometer by desorption electrospray ionization mass spectrometry. J Mass Spectrom **45**(2), 223–226 (2010)
43. Perdian, D.C., Schieffer, G.M., Houk, R.S.: Atmospheric pressure laser desorption/ionization of plant metabolites and plant tissue using colloidal graphite. Rapid Commun Mass Spectrom **24**(4), 397–402 (2010)
44. Sugiura, Y., Setou, M.: Imaging mass spectrometry for visualization of drug and endogenous metabolite distribution: toward in situ pharmacometabolomes. J. Neuroimmune Pharmacol. **5**(1), 31–43 (2010)
45. Hamm, G., Carre, V., Poutaraud, A., Maunit, B., Frache, G., Merdinoglu, D., Muller, J.F.: Determination and imaging of metabolites from *Vitis vinifera* leaves by laser desorption/ionisation time-of-flight mass spectrometry. Rapid Commun Mass Spectrom **24**(3), 335–342 (2010)
46. Goto-Inoue, N., Setou, M., Zaima, N.: Visualization of spatial distribution of gamma-aminobutyric acid in eggplant (*Solanum melongena*) by matrix-assisted laser desorption/ionization imaging mass spectrometry. Anal Sci **26**(7), 821–825 (2010)
47. Miura, D., Fujimura, Y., Yamato, M., Hyodo, F., Utsumi, H., Tachibana, H., Wariishi, H.: Ultrahighly sensitive in situ metabolomic imaging for visualizing spatiotemporal metabolic behaviors. Anal. Chem. **82**(23), 9789–9796
48. Svatos, A.: Mass spectrometric imaging of small molecules. Trends Biotechnol **28**(8), 425–434 (2010)
49. Jun, J.H., Song, Z.H., Liu, Z.J., Nikolau, B.J., Yeung, E.S., Lee, Y.J.: High-spatial and high-mass resolution imaging of surface metabolites of arabidopsis thaliana by laser desorption-ionization mass spectrometry using colloidal silver. Anal Chem **82**(8), 3255–3265 (2010)
50. Zaima, N., Hayasaka, T., Goto-Inoue, N., Setou, M.: Imaging of metabolites by MALDI mass spectrometry. J. Oleo Sci. **58**(8), 415–419 (2009)
51. Fernandez, J.A., Ochoa, B., Fresnedo, O., Giralt, M.T., Rodriguez-Puertas, R.: Matrix-assisted laser desorption ionization imaging mass spectrometry in lipidomics. Anal Bioanal Chem **401**(1), 29–51 (2011)
52. Hanrieder, J., Phan, N.T.N., Kurczy, M.E., Ewing, A.G.: Imaging mass spectrometry in neuroscience. ACS Chem Neurosci **4**(5), 666–679 (2013)

53. Kirsch, S., Zarei, M., Cindric, M., Muthing, J., Bindila, L., Peter-Katalinle, J.: On-line nano-HPLC/ESI QTOF MS and tandem MS for separation, detection, and structural elucidation of human erythrocytes neutral glycosphingolipid mixture. Anal Chem **80**(12), 4711–4722 (2008)
54. Milne, S.B., Mathews, T.P., Myers, D.S., Ivanova, P.T., Brown, H.A.: Sum of the parts: mass spectrometry-based metabolomics. Biochemistry **52**(22), 3829–3840 (2013)
55. Song, J., Liu, X.J., Wu, J.J., Meehan, M.J., Blevitt, J.M., Dorrestein, P.C., Milla, M.E.: A highly efficient, high-throughput lipidomics platform for the quantitative detection of eicosanoids in human whole blood. Anal Biochem **433**(2), 181–188 (2013)
56. Tulipani, S., Llorach, R., Urpi-Sarda, M., Andres-Lacueva, C.: Comparative analysis of sample preparation methods to handle the complexity of the blood fluid metabolome: when less is more. Anal Chem **85**(1), 341–348 (2013)
57. Garcia-Canaveras, J.C., Donato, M.T., Castell, J.V., Lahoz, A.: Targeted profiling of circulating and hepatic bile acids in human, mouse, and rat using a UPLC-MRM-MS-validated method. J Lipid Res **53**(10), 2231–2241 (2012)
58. Yan, X.J., Xu, J.L., Chen, J.J., Chen, D.Y., Xu, S.L., Luo, Q.J., Wang, Y.J.: Lipidomics focusing on serum polar lipids reveals species dependent stress resistance of fish under tropical storm. Metabolomics **8**(2), 299–309 (2012)
59. Gao, X.L., Zhang, Q.B., Meng, D., Isaac, G., Zhao, R., Fillmore, T.L., Chu, R.K., Zhou, J.Y., Tang, K.Q., Hu, Z.P., Moore, R.J., Smith, R.D., Katze, M.G., Metz, T.O.: A reversed-phase capillary ultra-performance liquid chromatography-mass spectrometry (UPLC-MS) method for comprehensive top-down/bottom-up lipid profiling. Anal Bioanal Chem **402**(9), 2923–2933 (2012)
60. Hellmuth, C., Weber, M., Koletzko, B., Peissner, W.: Nonesterified fatty acid determination for functional lipidomics: comprehensive ultrahigh performance liquid chromatography-tandem mass spectrometry quantitation, qualification, and parameter prediction. Anal Chem **84**(3), 1483–1490 (2012)
61. Henkels, K.M., Boivin, G.P., Dudley, E.S., Berberich, S.J., Gomez-Cambronero, J.: Phospholipase D (PLD) drives cell invasion, tumor growth, and metastasis in a human breast cancer xenograph model. Oncogene **32**(49), 5551–5562 (2013)
62. Kubo, A., Ohmura, M., Wakui, M., Harada, T., Kajihara, S., Ogawa, K., Suemizu, H., Nakamura, M., Setou, M., Suematsu, M.: Semi-quantitative analyses of metabolic systems of human colon cancer metastatic xenografts in livers of superimmunodeficient NOG mice. Anal Bioanal Chem **400**, 1895–1904 (2011)
63. van Hove, E.R.A., Blackwell, T.R., Klinkert, I., Eijkel, G.B., Heeren, R.M.A., Glunde, K.: Multimodal mass spectrometric imaging of small molecules reveals distinct spatio-molecular signatures in differentially metastatic breast tumor models. Cancer Res **70**, 9012–9021 (2010)
64. Allison, M.: Reinventing clinical trials. Nat. Biotech. **30**(1), 41–49 (2012)
65. Meacham, C.E., Morrison, S.J.: Tumor heterogeneity and cancer cell plasticity. Nature **501**(7467), 328–337 (2013)
66. Wu, Q., Li, M.Y., Li, H.Q., Deng, C.H., Li, L., Zhou, T.Y., Lu, W.: Pharmacokinetic-pharmacodynamic modeling of the anticancer effect of erlotinib in a human non-small-cell lung cancer xenograft mouse model. Acta Pharmacol Sin **34**(11), 1427–1436 (2013)
67. He, L., Guo, L., Vathipadiekal, V., Sergent, P. A., Growdon, W. B., Engler, D. A., Rueda, B.R., Birrer, M.J., Orsulic, S., Mohapatra, G.: Identification of LMX1B as a novel oncogene in human ovarian cancer. Oncogene (2013). doi:10.1038/onc.2013.375
68. Junttila, M.R., de Sauvage, F.: J.: Influence of tumour micro-environment heterogeneity on therapeutic response. Nature **501**(7467), 346–354 (2013)
69. Richmond, A., Su, Y.J.: Mouse xenograft models versus GEM models for human cancer therapeutics. Disease Models Mechanisms **1**(2/3), 78–82 (2008)
70. Fan, C.W., Chen, T., Shang, Y.N., Gu, Y.Z., Zhang, S.L., Lu, R., OuYang, S.R., Zhou, X., Li, Y., Meng, W.T., Hu, J.K., Lu, Y., Sun, X.F., Bu, H., Zhou, Z.G., Mo, X.M.: Cancer-initiating cells derived from human rectal adenocarcinoma tissues carry mesenchymal phenotypes and resist drug therapies. Cell Death Dis **4**, e828 (2013)
71. Chen, J., Bi, H., Hou, J., Zhang, X., Zhang, C., Yue, L., Wen, X., Liu, D., Shi, H., Yuan, J., Liu, J., Liu, B.: Atorvastatin overcomes gefitinib resistance in KRAS mutant human non-small cell lung carcinoma cells. Cell Death Dis. **4**, e814 (2013)
72. Holohan, C., Van Schaeybroeck, S., Longley, D.B., Johnston, P.G.: Cancer drug resistance: an evolving paradigm. Nat Rev Cancer **13**(10), 714–726 (2013)
73. Kelley, R.K., Hwang, J., Magbanua, M.J.M., Watt, L., Beumer, J.H., Christner, S.M., Baruchel, S., Wu, B., Fong, L., Yeh, B.M., Moore, A.P., Ko, A.H., Korn, W.M., Rajpal, S., Park, J.W., Tempero, M.A., Venook, A.P., Bergsland, E.K.: A Phase 1 trial of imatinib, bevacizumab, and metronomic cyclophosphamide in advanced colorectal cancer. Br J Cancer **109**(7), 1725–1734 (2013)
74. Jensen, M., Jorgensen, J., Binderup, T., Kjaer, A.: Tumor volume in subcutaneous mouse xenografts measured by microCT is more accurate and reproducible than determined by 18F-FDG-microPET or external caliper. BMC Med Imaging **8**(1), 16 (2008)
75. Bligh, E.G., Dyer, W.J.: A rapid method of total lipid extraction and purification. Can. J. Biochem. Physiol. **37**(8), 911–917 (1959)
76. Astigarraga, E., Barreda-Gomez, G., Lombardero, L., Fresnedo, O., Castano, F., Giralt, M.T., Ochoa, B., Rodriguez-Puertas, R., Fernandez, J.A.: Profiling and imaging of lipids on brain and liver tissue by matrix-assisted laser desorption/ionization mass spectrometry using 2-mercaptobenzothiazole as a matrix. Anal Chem **80**(23), 9105–9114 (2008)
77. Hankin, J.A., Barkley, R.M., Murphy, R.C.: Sublimation as a method of matrix application for mass spectrometric imaging. J Am Soc Mass Spectrom **18**(9), 1646–1652 (2007)
78. Yang, J.H., Caprioli, R.M.: Matrix sublimation/recrystallization for imaging proteins by mass spectrometry at high spatial resolution. Anal Chem **83**(14), 5728–5734 (2011)
79. Deininger, S.O., Cornett, D.S., Paape, R., Becker, M., Pineau, C., Rauser, S., Walch, A., Wolski, E.: Normalization in MALDI-TOF imaging datasets of proteins: practical considerations. Anal Bioanal Chem **401**(1), 167–181 (2011)
80. Xiong, X.C., Xu, W., Eberlin, L.S., Wiseman, J.M., Fang, X., Jiang, Y., Huang, Z.J., Zhang, Y.K., Cooks, R.G., Ouyang, Z.: Data processing for 3D mass spectrometry imaging. J Am Soc Mass Spectrom **23**(6), 1147–1156 (2012)
81. Wold, S., Esbensen, K., Geladi, P.: Principal component analysis. chemometrics intel. Lab. Syst. **2**(1/3), 37–52 (1987)
82. Arthur, D., Vassilvitskii, S. k-Means++: the advantages of careful seeding. Society Industrial Applied Mathematics: New Orleans, LA; pp. 1027–1035 (2007)
83. Zemski Berry, K.A., Hankin, J.A., Barkley, R.M., Spraggins, J.M., Caprioli, R.M., Murphy, R.C.: MALDI imaging of lipid biochemistry in tissues by mass spectrometry. Chem Rev **111**(10), 6491–6512 (2011)
84. Fhaner, C.J., Liu, S., Ji, H., Simpson, R.J., Reid, G.E.: Comprehensive lipidome profiling of isogenic primary and metastatic colon adenocarcinoma cell lines. Anal Chem **84**(21), 8917–8926 (2012)
85. Yang, H.J., Park, K.H., Lim, D.W., Kim, H.S., Kim, J.: Analysis of cancer cell lipids using matrix-assisted laser desorption/ionization 15-T Fourier transform ion cyclotron resonance mass spectrometry. Rapid Commun Mass Spectrom **26**(6), 621–630 (2012)
86. Smith, R., Lespi, P., Di Luca, M.A., Bustos, C., Marra, F., Alaniz, M.A., Marra, C.: A reliable biomarker derived from plasmalogens to evaluate malignancy and metastatic capacity of human cancers. Lipids **43**(1), 79–89 (2008)
87. Zang, F., Du, G.: Dysregulated lipid metabolism in cancer. World J. Biol. Chem. **3**(8), 167–174 (2013)
88. Hankin, J., Farias, S., Barkley, R., Heidenreich, K., Frey, L., Hamazaki, K., Kim, H.Y., Murphy, R.: MALDI mass spectrometric imaging of lipids in rat brain injury models. J Am Soc Mass Spectrom **22**(6), 1014–1021 (2011)